

CardioComposer: Flexible and Compositional Anatomical Structure Generation with Disentangled Geometric Guidance

Karim Kadry¹Shoaib Goraya²Farhad R. Nezami²Ajay Manicka¹Abdalla Abdelwahed³Elazer R. Edelman¹

Abstract

Generative models of 3D anatomy, when integrated with biophysical simulators, enable the study of structure-function relationships for clinical research and medical device design. However, current models face a trade-off between controllability and anatomical realism. We propose a programmable and compositional framework for guiding unconditional diffusion models of human anatomy using interpretable ellipsoidal primitives embedded in 3D space. Our method involves the selection of certain tissues within multi-tissue segmentation maps, upon which we apply geometric moment losses to guide the reverse diffusion process. This framework supports the independent control over size, shape, and position, as well as the composition of multi-component constraints during inference.

1 Introduction

Three-dimensional segmentations of human anatomy power a variety of physics-based simulation platforms. For example, virtual cohorts of anatomy can be used for virtual clinical trials to evaluate and optimize novel medical devices and imaging systems [1–3]. Additionally, biophysical simulations can generate insights in the context of both computational physiology research [4–6], and surgical training [7]. Anatomical segmentations can also be used to augment machine-learning workflows through simulating the formation of synthetic images, either through physics-based models [8, 9], domain randomization [10, 11], or using anatomy-controlled generative models [12, 13].

Using generative models of anatomy as a surrogate data source for simulation platforms offers several advantages over using patient-data alone. For example, conditional generation can augment computational trial cohorts with anatomical variants that are both novel

and rare [14]. Moreover, generative editing methods such as inpainting can precisely modify existing patient geometry to create anatomically plausible variations [15, 16]. These “digital siblings” can be used with biophysical simulators to model *counterfactual* scenarios that elucidate the relationship between anatomical form and function.

However, unlike generative modeling of 3D shapes for artistic purposes, generating anatomical models for biophysical simulations presents several unique challenges. The first challenge relates to *scale-critical* features, where minor geometric variations on the order of mere millimeters can cause major fluctuations in physiological behavior [17–19]. Second, anatomical structure exerts *attribute-specific* effects, where features such as size and position play differing roles in determining biophysical outcomes [20]. Lastly, multiple components or tissues interact in a *compositional* manner [20–22], where the relative arrangement and properties of adjacent structures collectively influence simulation results. These challenges highlight the essential functionalities for anatomical generative models, namely: that they can precisely control critical geometric attributes, independently manipulate different attributes such as size or shape, and control the geometry of multiple components in a compositional manner.

To address these design requirements, we present CardioComposer, a novel framework for guiding unconditional diffusion models using interpretable ellipsoidal primitives that represent geometric attributes such as size, shape, and position (Figure 1A). Our guidance framework allows for independent control of size, shape, and position (Figure 1B-D), as well as the ability to compose geometric constraints for arbitrary numbers of anatomical components (Figure 1E-G). Our *key insight* is that a linear combination of simple loss functions applied to target and predicted geometric features can jointly constrain anatomical generation. We demonstrate this method on multi-tissue cardiovascular segmentations, which exhibit a wide array of structures such as star-shaped chambers, and tubular vasculature.

¹Massachusetts Institute of Technology

²Brigham and Women’s Hospital

³American University in Cairo

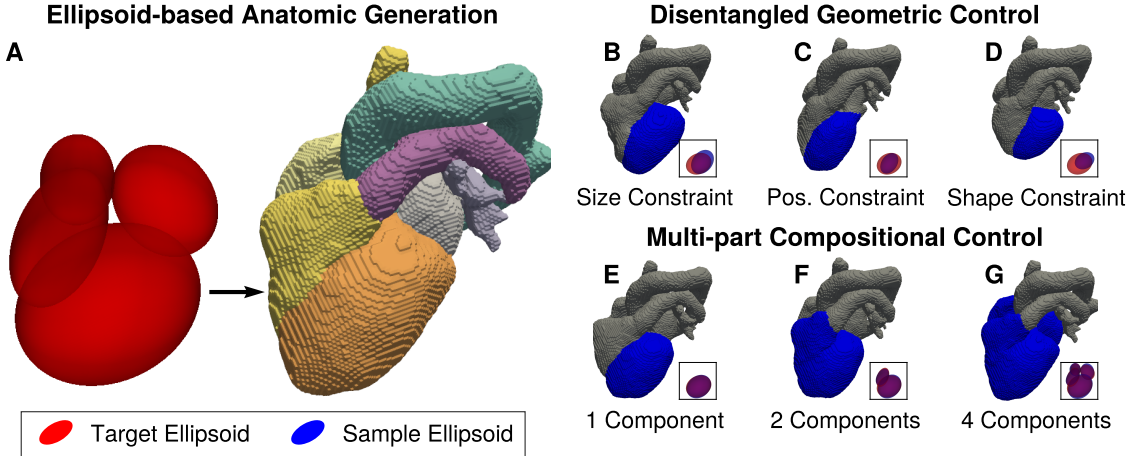


Figure 1: We present a guidance framework to constrain diffusion models of multi-label anatomical segmentations based on simple geometric features. We specifically guide the model with interpretable and editable features that can represent ellipsoids in 3D space, such as size, shape, and position (panel A). Our approach does not require model re-training, enables the independent generation of anatomy based on various geometric features (panels B-D), and supports multi-component compositional generation (panels E-G). For panels B-G, gray \blacksquare and blue \blacksquare voxels represent components that are unconstrained and constrained, respectively, and purple ellipsoids $\textcolor{purple}{\bullet}$ indicate a strong overlap between target $\textcolor{red}{\bullet}$ and sample ellipsoids $\textcolor{blue}{\bullet}$.

Our key contributions include the following:

- We reformulate geometrically constrained synthesis of 3D anatomical segmentations in terms of guiding unconditional diffusion models with a differentiable geometric loss at inference.
- We develop a composite geometric loss function enabling *independent* control over size, shape, and position.
- We apply such geometric losses to individual tissues within the anatomical segmentation, enabling *multi-part* compositional generation.

2 Background

Traditional Morphometric Modeling for Anatomy. Anatomical modeling involves digitally quantifying and representing anatomical structures through geometric measurements. Traditional morphometric approaches characterize anatomy through intrinsic factors such as length, area, volume, and shape, as well as extrinsic factors such as position and orientation. These measurements are often performed in specialized coordinate systems adapted to specific anatomical contexts; curvilinear coordinates for vascular trees [23], polar coordinates for valves [24], and custom coordinate systems for biventricular geometries

[25]. Geometric measurements enable various clinical applications, including cardiovascular risk stratification [26, 27], orthopedic diagnosis [28], and radiomics-based prognosis [29]. However, traditional morphometric modeling faces two key challenges: it cannot capture complex nonlinear correlations between features, and multiple distinct anatomies may map to the same high-level measurements. To address these limitations, we propose a framework in which an unconditional diffusion model is controlled by traditional morphometric features (size, shape, position) to generate a wide variety of realistic anatomical structures, providing an approachable anatomical modeling interface for both clinical and engineering workflows that involve numerical simulation.

Generative Models for Numerical Simulation. Anatomical modeling serves as a crucial tool for both studying form-function relationships and enabling physical simulations for scientific discovery and medical device design. Current approaches span a spectrum of complexity and control, yet each faces fundamental limitations. Simple geometric primitives, such as cylinders for coronary arteries [30–32] and truncated ellipsoids for cardiac chambers [33] offer parametric control but fail to capture anatomical realism. Data-driven approaches like statistical shape models and autoencoders [14, 34–38] can represent anatomy in terms of a global shape vector, where each element corresponds to composite

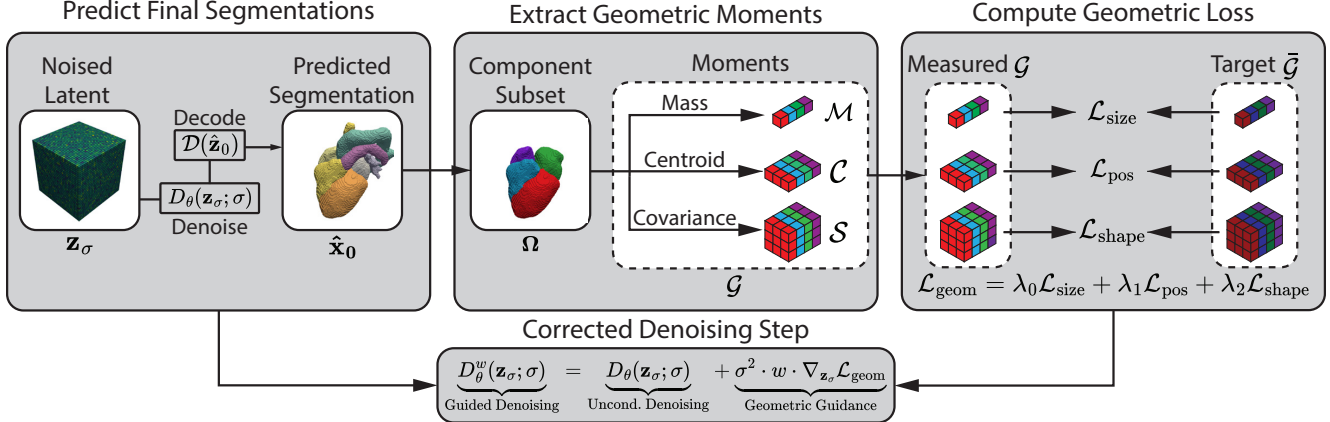


Figure 2: **Our method involves applying a geometric guidance correction step for every denoising iteration.** Left: the noised latent \mathbf{z}_σ is passed through the diffusion model and VAE decoder to produce a clean voxel space prediction $\hat{\mathbf{x}}_0$ (Section 4.2). Middle: The segmentation is filtered for components of interest Ω , and geometric moments \mathcal{G} are extracted per component (Section 4.3). Right: the measured geometric moments \mathcal{G} are compared to target moments $\bar{\mathcal{G}}$ through geometric moment losses, and are aggregated to produce a final loss that can be used to guide sampling by taking the gradient (Section 4.4). Bottom: The gradient derived from the geometric loss is then used to adjust the denoising step.

shape factors. Data-driven approaches have recently been utilized to generate synthetic data for mechanistic studies of heart disease [39, 40] and engineering design [41], but are limited in terms of modeling fine-grained geometric attributes. Similarly, physics-based deformation methods [42, 43] allow precise control of vessel geometry through cross-sectional modifications, but are limited to modifying existing patient anatomy. Recent diffusion-based approaches have been used to precisely edit patient-specific models to create ‘anatomical digital siblings’ [15], enabling perturbations and inpainting of cardiac geometries. However, such edits induced undesirable morphological bias when applied to rare and pathological cases. To this end, several studies have examined how to condition generative models of anatomy on anatomical features through explicitly provided scalar features as conditional variables during training. For example, de Wilde et al. [44] trained a conditional generative model on thyroid segmentations, and Kadry et al. [16] developed morpho-skeletal control mechanisms for coronary arteries through null-guidance and loss-based approaches. However, both approaches critically rely on conditionally training generative models and primarily restrict themselves to conditioning variables related to size such as volume or cross-sectional area. In contrast, we develop a general inference-time framework that can control an unconditional diffusion model with a wide range of traditional morphometric features such as size, shape, and position.

Spatial Control of Generative Models. Spatial

control of generative models is achieved through two principal approaches with distinct tradeoffs. The first approach conditions models on interpretable mid-level representations (e.g., bounding boxes, ellipsoid parameters) and has been successfully applied to images [45], video [46], 3D objects [47, 48], and biological structures [49]. However, these methods cannot accommodate novel constraints during inference as they depend on training conditional models for every constraint. The second approach employs gradient-based guidance during the reverse diffusion process [50, 51], enabling flexible constraint composition at test time, but typically limited to general localization rather than precise geometric control. Recent work such as self-guidance leverages attention-based loss functions to enable basic geometric attribute control (size, position) in text-to-image models [52], but does not control for orientation or aspect ratio. In our work, we extend loss-based guidance by introducing geometric losses to 3D multi-component anatomical segmentations based on label-wise geometric properties such as the mass, centroid, and covariance, enabling the composition of multiple constraints across constraint type (mass vs. centroid) as well as several components.

3 Anatomical Diffusion Models

Let $\mathbf{x} \in \mathbb{R}^{C \times H \times W \times D}$ be a 3D segmentation volume with C tissue channels and (H, W, D) spatial dimensions. We employ a variational autoencoder (VAE), which con-

sists of an encoder \mathcal{E} and decoder \mathcal{D} , to map \mathbf{x} to a lower-dimensional latent representation $\mathbf{z} \in \mathbb{R}^{c \times h \times w \times d}$ with c channels and spatial dimensions (h, w, d) where $(h, w, d) = (H/f, W/f, D/f)$ for an integer downsampling factor f :

$$\mathbf{z} = \mathcal{E}(\mathbf{x}) \quad \text{and} \quad \hat{\mathbf{x}} = \mathcal{D}(\mathbf{z}). \quad (1)$$

We use an unconditional latent diffusion model (LDM) as a prior for 3D anatomical segmentations, trained on the encoded latent representations \mathbf{z} . In the forward process, data samples $\mathbf{z} \sim p_{\text{data}}(\mathbf{z})$ are progressively corrupted by adding Gaussian noise, resulting in noised data $\mathbf{z}_\sigma = \mathbf{z} + \mathbf{n}$ where $\mathbf{n} \sim \mathcal{N}(\mathbf{0}, \sigma^2 \mathbf{I})$. The reverse process reconstructs the original data by approximating the score function $\nabla_{\mathbf{z}_\sigma} \log p(\mathbf{z}_\sigma; \sigma)$, which directs the denoising trajectory towards higher data density regions. This score function is modeled using the denoiser model D_θ , such that

$$\nabla_{\mathbf{z}_\sigma} \log p(\mathbf{z}_\sigma; \sigma) = \frac{D_\theta(\mathbf{z}_\sigma; \sigma) - \mathbf{z}_\sigma}{\sigma^2}.$$

The reverse sampling process is governed by the stochastic differential equation

$$d\mathbf{z}_\sigma = -2\sigma \nabla_{\mathbf{z}_\sigma} \log p(\mathbf{z}_\sigma; \sigma) dt + \sqrt{2\sigma} d\mathbf{w},$$

where $d\mathbf{w}$ is the Wiener process. The model is trained by minimizing the clean data prediction objective

$$L = \mathbb{E}_{\sigma, \mathbf{z}, \mathbf{n}} [\lambda(\sigma) \|D_\theta(\mathbf{z}_\sigma; \sigma) - \mathbf{z}\|_2^2],$$

with $\lambda(\sigma)$ balancing loss contributions across noise levels.

4 Geometric Guidance

4.1 Overview

Our objective is to direct an unconditional diffusion model trained on 3D multi-component anatomical segmentations to satisfy geometric constraints without requiring additional training. Such constraints should apply to each individual *component* and involve the independent control of size, position, and shape. We formulate this problem in terms of guiding the diffusion model sampling process with a composite *geometric loss* applied to a select subset of segmentation labels (defined as components). This geometric loss is a weighted sum of moment-based terms that directly translate to anatomical features: size is represented as zeroth-order moments (volume of present labels), position as first-order moments (3D centroid), and shape as second-order moments (covariance) that are scale-normalized. Algorithm 1 and Figure 2 illustrate the geometric guidance

Algorithm 1 Geometric Guidance

```

Require:  $\sigma, \mathbf{z}_\sigma, \bar{\mathcal{G}}$ 
1:  $\hat{\mathbf{z}}_0 \leftarrow D_\theta(\mathbf{z}_\sigma; \sigma)$  {Denoise Latents}
2:  $\hat{\mathbf{x}}_0 \leftarrow \mathcal{D}(\hat{\mathbf{z}}_0)$  {Decode Voxels}
3:  $\boldsymbol{\Omega} \leftarrow \mathbf{T}_\Omega(\hat{\mathbf{x}}_0)$  {Select Components}
4:  $\mathcal{G} \leftarrow \mathbf{T}_G(\boldsymbol{\Omega})$  {Geometric Moment Extraction}
5:  $\mathcal{L}_{\text{geom}} \leftarrow \mathcal{L}(\mathcal{G}, \bar{\mathcal{G}})$  {Compute Moment Loss}
6: return  $\nabla_{\mathbf{z}_\sigma} \mathcal{L}_{\text{geom}}$  {Compute Gradient}

```

process, which consists of four main stages. First, we denoise and decode the anatomical segmentation during sampling. Second, we select the desired anatomical components $\boldsymbol{\Omega}$ and extract the set of geometric moments $\mathcal{G} = [\mathcal{M}, \mathcal{C}, \mathcal{S}]$, representing the mass, centroid, and covariance for each component. Third, we compute the geometric loss $\mathcal{L}_{\text{geom}}$ with respect to target moments $\bar{\mathcal{G}}$ obtained by real anatomies or manual editing. Lastly, the gradient of this loss with respect to the noisy latents is used to guide the sampling process.

4.2 Segmentation Denoising and Guidance

We formulate loss-based guidance in similar terms to diffusion posterior sampling [53], where the gradient derived from a differentiable geometric loss $\mathcal{L}_{\text{geom}}$ guides the sampling process. To guide anatomical generation, the intermediately noised latent \mathbf{z}_σ is denoised by the diffusion model to produce a clean prediction $\hat{\mathbf{z}}_0 = D_\theta(\mathbf{z}_\sigma; \sigma)$ and subsequently decoded into a voxel-space segmentation $\hat{\mathbf{x}}_0 = \mathcal{D}(\hat{\mathbf{z}}_0)$. To ensure that the segmentation yields appropriate measures of geometric features, we apply a label-wise softmax with a low temperature value to ensure that the segmentation values are close to binary. We then use the clean data prediction to compute the geometric loss $\mathcal{L}_{\text{geom}}$ in a differentiable manner and update the denoiser predictions through the gradient with respect to the noised latent \mathbf{z}_σ . We finally parametrize the update step with a general guidance weight w as follows:

$$\underbrace{D_\theta^w(\mathbf{z}_\sigma; \sigma)}_{\text{Guided Denoising}} = \underbrace{D_\theta(\mathbf{z}_\sigma; \sigma)}_{\text{Uncond. Denoising}} - \underbrace{\sigma^2 \cdot w \cdot \nabla_{\mathbf{z}_\sigma} \mathcal{L}_{\text{geom}}}_{\text{Geometric Guidance}} \quad (2)$$

4.3 Geometric Moments Extraction

To isolate guidance to a selected subset of tissue labels, we apply the **component filtration** function, $\mathbf{T}_\Omega(x)$, which maps the input segmentation $\hat{\mathbf{x}}_0 \in \mathbb{R}^{C \times H \times W \times D}$ to a subset of the original segmentation $\boldsymbol{\Omega} \in \mathbb{R}^{E \times H \times W \times D}$. Here, E specifies the subset of channels considered for applying constraints.

To extract geometric features, we apply a geometric measurement function $\mathbf{T}_G(\Omega)$ to compute the set of geometric moments $\mathcal{G} = [\mathcal{M}, \mathcal{C}, \mathcal{S}]$, where $\mathcal{M} \in \mathbb{R}^{E \times 1}$ represents the masses or volumes for each label, $\mathcal{C} \in \mathbb{R}^{E \times 3}$ represents the centroids, and $\mathcal{S} \in \mathbb{R}^{E \times 3 \times 3}$ represents the covariances. Specifically, for each component k , we define $\Omega_k \in \mathbb{R}^{(H \times W \times D) \times 1}$ as the flattened voxel grid and $\mathbf{p} \in \mathbb{R}^{(H \times W \times D) \times 3}$ as the normalized voxel coordinates between 0 and 1. We compute the geometric moments as

$$\mathcal{M}_k = \mathbf{1}^T \cdot \Omega_k \quad \text{and} \quad \mathcal{C}_k = \frac{\Omega_k^T \mathbf{p}}{\mathcal{M}_k} \quad (3)$$

$$\mathcal{S}_k = \frac{1}{\mathcal{M}_k} \mathbf{p}^T \text{diag}(\Omega_k) \mathbf{p} - \mathcal{C}_k^T \mathcal{C}_k \quad (4)$$

where $\mathbf{1}^T$ is the all-ones vector, and $\text{diag}(\cdot)$ refers to diagonal matrix embedding. To enable independent control over size and shape characteristics, we compute a normalized representation of the covariance matrix. The scale-normalized covariance matrix is defined as $\mathcal{S}^n = \frac{\mathcal{S}}{\text{tr}(\Lambda)}$ where Λ is the eigenvalue matrix obtained from the eigendecomposition of \mathcal{S} .

4.4 Geometric Loss Computation

Following the computation of geometric moments, we calculate individual loss terms by comparing each moment to its corresponding target moment $\bar{\mathcal{G}} = [\bar{\mathcal{M}}, \bar{\mathcal{C}}, \bar{\mathcal{S}}^n]$. For each geometric feature, we compute the mean squared error (MSE) between the measured and target values. These individual loss terms are defined as:

$$\mathcal{L}_{\text{size}} = \mathcal{L}_{\text{MSE}}(\mathcal{M}, \bar{\mathcal{M}}) \quad (5)$$

$$\mathcal{L}_{\text{pos}} = \mathcal{L}_{\text{MSE}}(\mathcal{C}, \bar{\mathcal{C}}) \quad (6)$$

$$\mathcal{L}_{\text{shape}} = \mathcal{L}_{\text{MSE}}(\mathcal{S}^n, \bar{\mathcal{S}}^n) \quad (7)$$

Using prescribed weight factors $\lambda_0, \lambda_1, \lambda_2$, we compute the geometric loss as

$$\mathcal{L}_{\text{geom}} = \lambda_0 \mathcal{L}_{\text{size}} + \lambda_1 \mathcal{L}_{\text{pos}} + \lambda_2 \mathcal{L}_{\text{shape}}.$$

The weighted sum and individual weights λ_i , allow us to control the contribution of individual loss to the guidance process, enabling easy disentangled control by zeroing out the associated weighting factor.

5 Experiments

5.1 Dataset

We used the TotalSegmentator dataset [54], consisting of 1204 computed tomography (CT) images. We extract

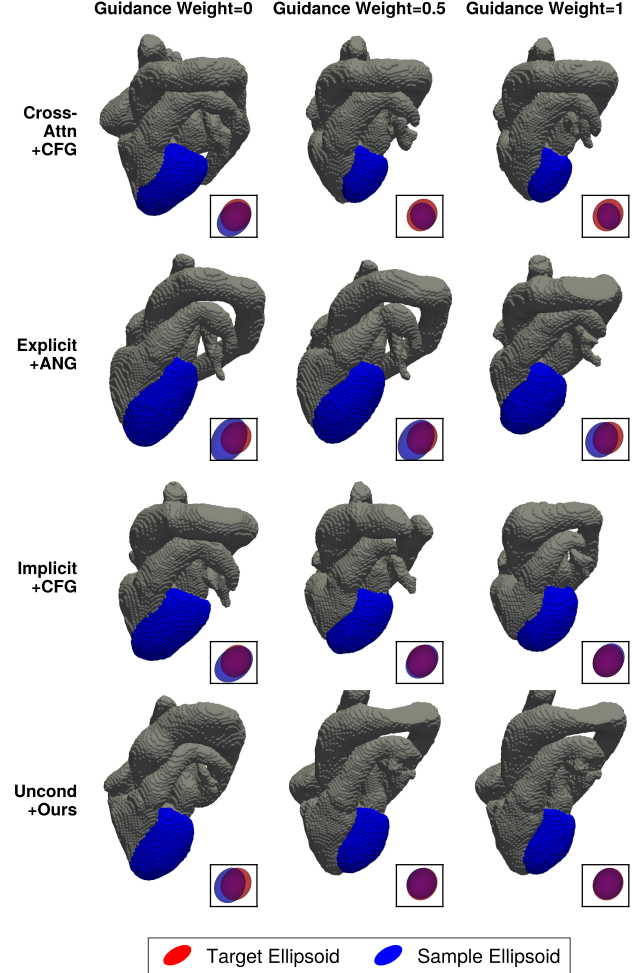


Figure 3: Geometric guidance enables the generation of synthetic anatomy with geometric constraints. Grid shows example synthetic label maps where the constraints are applied to the myocardium voxels ■. Columns: guidance weights. Rows: baseline conditioning and guidance methods, where CFG refers to classifier-free guidance and ANG refers to adaptive null guidance.

all labels related to the heart, which include aorta (Ao), pulmonary artery (PA), pulmonary veins (PV), inferior vena cava (IVC), superior vena cava (SVC), left atrium (LA), right atrium (RA), left ventricle (LV), and right ventricle (RV), and left ventricular myocardium (Myo). Lastly, we manually filter out low-quality label maps and apply one-hot encoding, resulting in a dataset of 596 3D cardiac segmentations with 11 channels and an isotropic voxel edge length of 2 mm. See Section 8.2 for further details. We split the dataset into training and validation sets with an 80/20 split, where all target moments and evaluation metrics are computed on the

validation set.

5.2 Unconditional Training and Guidance

We train an unconditional diffusion model on cardiac label maps similarly to Kadry et al. [15]. We use a convolutional VAE to compress the voxel-space segmentation into a latent representation by a factor of four and train a diffusion model denoiser that consists of a convolutional U-Net with self-attention layers (further details in Section 8.3). To compute our geometric guidance loss, we take the weighted sum of the individual geometric moment losses, where the guidance weights λ_i are tuned experimentally (see Section 8.4).

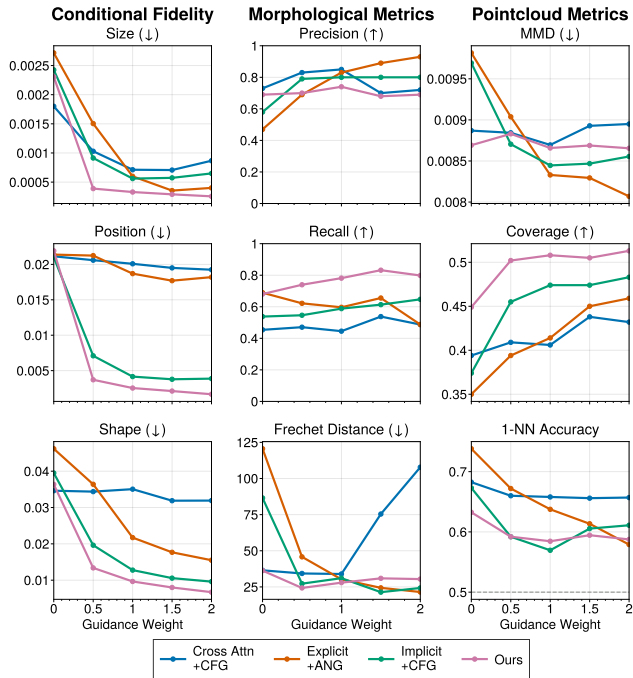


Figure 4: Geometric guidance exhibits a strong trade-off between conditional control and anatomical realism. Line plots compare conditioning and guidance mechanisms based on the geometric properties of the myocardium. Left column: improved conditional fidelity for size, shape, and position. Middle column: controlling generation with our method improves morphological quality and pointcloud metrics. Right column: our method also improves pointcloud-based metrics.

5.3 Baselines

We compare our approach (unconditional diffusion combined with geometric guidance) to conditional training

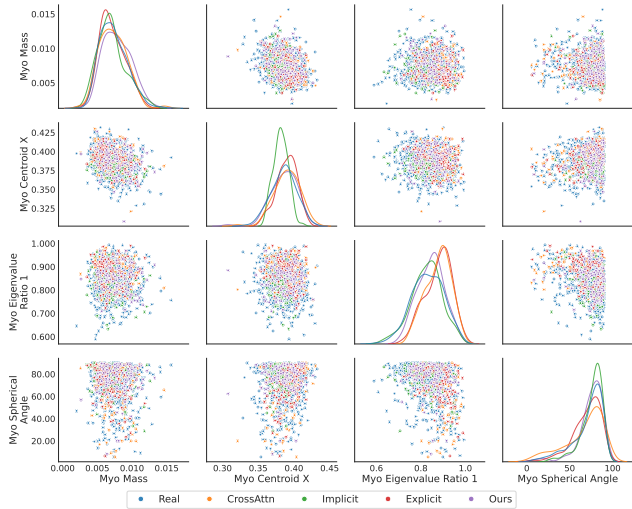


Figure 5: Geometric guidance can help recapitulate morphological distributions. Pair plot shows kernel density estimate plots (diagonals) and pairwise scatterplots (off-diagonals) for various morphological metrics. We plot the morphological metrics for anatomies generated through conditional generation baselines and geometric guidance (ours). In this plot, the myocardium is being constrained.

approaches. Given the geometric moments representing the size \mathcal{M} , centroid \mathcal{C} and covariance \mathcal{S} of each cardiac component, we condition the model in the following ways:

- **Explicit Concatenation:** This approach encodes geometric attributes in the values of the conditioning signal [16]. Here, we adapt this method to positional and shape-based features. We flatten and stack all geometric moments into a vector for all E components. We then expand this vector into a voxel grid $\mathcal{G}_{\text{exp}} \in \mathbb{R}^{(1+3+E) \times h \times w \times d}$ which is concatenated to the latents along the channel dimension.

- **Implicit Concatenation:** This approach indirectly encodes geometric attributes in the conditioning signal through 3D heatmaps [16]. Here, we embed geometric moments as 3D Gaussians in voxel space. For each component, we create a voxel-map $\mathcal{G}_{\text{imp}} \in \mathbb{R}^{E \times h \times w \times d}$ where the voxel values encode the Mahalanobis distance to the approximating ellipsoid for each component.

- **Cross-attention:** We express the conditioning signal as a sequence of tokens where each token represents a component and the dimension of each

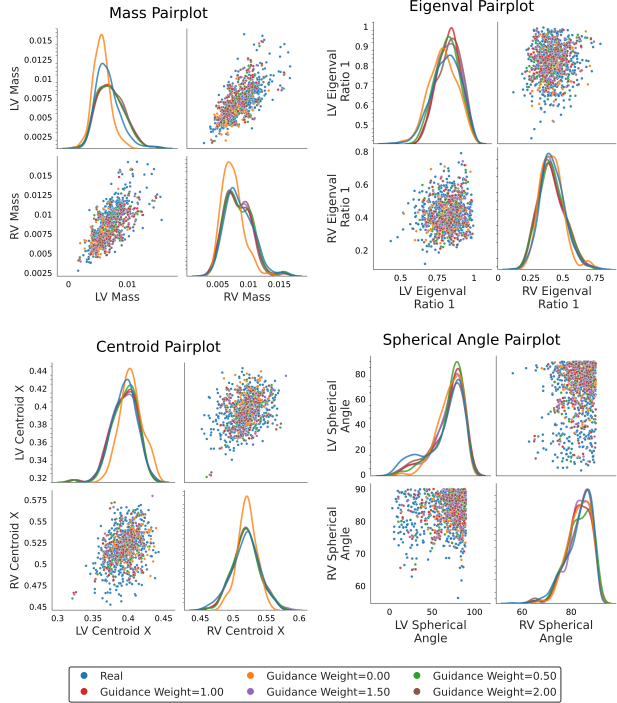


Figure 6: Geometric guidance improves morphological distribution similarity between real and synthetic anatomy. Pair plot shows morphological relationships for mass (top left panel), centroid (bottom left panel), ellipsoidal axis lengths (top right panel) and orientation (bottom right panel), where the myocardium labels are being constrained. For each panel, diagonal plots show kernel density estimates for component-specific metrics (LV and RV) and off-diagonal plots show pairwise scatter plots between components.

token corresponds to the embedded geometric moments $\mathcal{G}_{\text{cross}} \in \mathbb{R}^{E \times 256}$. To enable sequence conditioning for the denoising U-Net, we convert the self-attention layers to cross-attention layers, similar to modern text-to-image diffusion models [55].

We further implement guidance mechanisms such as adaptive null guidance (ANG) [16] for explicit concatenation, and classifier-free guidance (CFG) [56] for implicit concatenation and cross-attention. Further details can be found in Section 8.5.

5.4 Evaluation Metrics

We evaluate pairwise conditional fidelity for size, shape, and position by taking the L_1 -norm between the target moments and the sample moments. We further measure morphological quality metrics that compare

the distribution of real and synthetic anatomy in morphological vector space [15]. To embed each anatomy within morphological space, we concatenate the masses, centroids, and eigenvalues of the normalized covariance matrix for all 10 anatomical labels. We specifically use morphological variants of improved precision and recall, as well as the Fréchet distance (FD) [15, 57]. Lastly, we leverage the pointcloud-based metrics used in 3D shape-generation literature [58], consisting of minimum matching distance (MMD), coverage (COV) and 1-nearest neighbor accuracy (1-NNA). Distances between pointclouds are computed as the Earth Mover’s Distance (EMD). Further details can be found in Section 8.6.

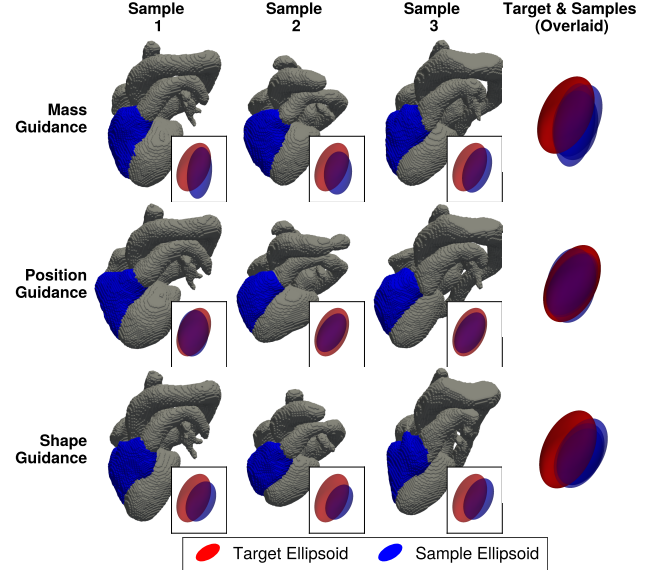


Figure 7: Geometric guidance enables independent control of size, shape, and position. Columns show synthetic label maps generated by geometric guidance applied to the right ventricle voxels ■ using various geometric losses. Rows represent which geometric feature is being independently controlled. The final column shows the target and several sample ellipsoids superimposed.

5.5 Evaluating Anatomical Generation Quality

We first aim to compare and evaluate the effect of geometric conditioning and guidance on both conditional fidelity and synthetic anatomy quality. We sample target moments for a single component (myocardium) from the validation set and generate 200 anatomical segmentations for our method and all baselines. We sweep over

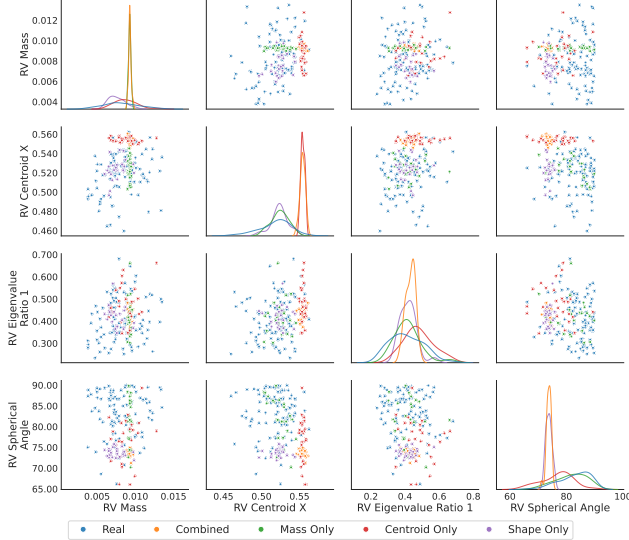


Figure 8: **Geometric guidance enables independent control of size, shape, and position.** Pair plot shows kernel density estimate plots (diagonals) and pairwise scatterplots (off-diagonals) of various morphological metrics. Guidance is applied to control various features of the right ventricle. By sampling several anatomies from the same target moments, we can independently constrain morphological metrics (represented by tall and peaked kernel density plots) but keep other metrics free to vary between samples. Morphological metrics for real anatomies are subsampled for visual clarity.

general guidance weights $w \in [0, 2]$, where 0 corresponds to unconditional sampling. In Figure 4, we show that geometric guidance enhances conditional fidelity, especially at higher guidance weights. We observe that our method does not suffer in terms of generation quality, retaining similar levels of morphological and pointcloud evaluation metrics with increasing guidance. Figure 3 shows example label maps generated through varying guidance values for all methods. We observe that only our method and implicit conditioning properly align the target and sample ellipsoids with increasing guidance weights. In Figure 6, we show that geometric guidance better aligns the distribution of geometric features when comparing real and synthetic anatomy. Figure 5 shows that all geometric-control methods can recapitulate the morphological distribution exhibited by the real data. Further information on which geometric features were plotted can be found in Section 8.8.

5.6 Evaluating Geometric Disentanglement

We next show how our guidance framework uniquely enables disentangled geometric control. We evaluate geometric disentanglement using 100 target moments for myocardial labels from the validation set using no losses (Uncond.), a combination of all losses ($\mathcal{L}_{\text{geom}}$), or each individual moment loss ($\mathcal{L}_{\text{size}}$, \mathcal{L}_{pos} , and $\mathcal{L}_{\text{shape}}$). Table 1 and Figure 9 show that using the individual losses improves their respective conditional fidelity but does not affect the other conditional fidelity metrics. Using the individual losses produces similar conditional fidelity metrics for their target geometric feature in comparison to the combined geometric loss. Moreover, the Fréchet distance is improved when using any loss, while 1-NNA is only improved for the full geometric loss and positional losses. Qualitative results can be seen in Figures 7 and 8, where the right ventricle is constrained independently by mass, position, or shape. Mass guidance, for example, produces right ventricles with roughly the same size as the target, but vary with respect to shape and position.

Table 1: **Ablation study showing disentangled geometric guidance results for size, shape, and positional losses.** Uncond. represents geometric guidance with all loss weights deactivated, $\mathcal{L}_{\text{geom}}$ represents the linear combination of all losses. For ease of visualization, conditional fidelity values for size are multiplied by 10^4 , while centroid and shape values are multiplied by 10^3 .

Guidance Loss	Cond. Fidelity			Gen. Qual.	
	Size	Position	Shape	FD	NNA
Uncond.	20.0	23.6	34.9	36.5	0.64
$\mathcal{L}_{\text{size}}$	3.3	20.0	33.1	32.7	0.64
\mathcal{L}_{pos}	18.4	2.5	30.9	35.7	0.60
$\mathcal{L}_{\text{shape}}$	17.5	21.4	9.7	34.4	0.65
$\mathcal{L}_{\text{geom}}$	3.3	2.48	9.5	28.4	0.59

5.7 Evaluating Multi-Component Compositionality

We aim to compare and evaluate the capability of our method to achieve multi-part control, where the model can be constrained based on an arbitrary combination of components. We sample 100 target moments from the validation set and aim to constrain generation based on: (a) only the myocardium (1 component), (b) the right heart labels (3 components), and (c) both right

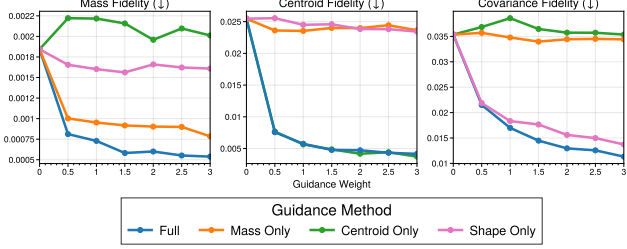


Figure 9: **Geometric guidance enables independent control of size, shape, and position.** Line-plots compare conditional fidelity when using geometric guidance with individual losses for mass, position, and shape, as well as all losses in tandem.

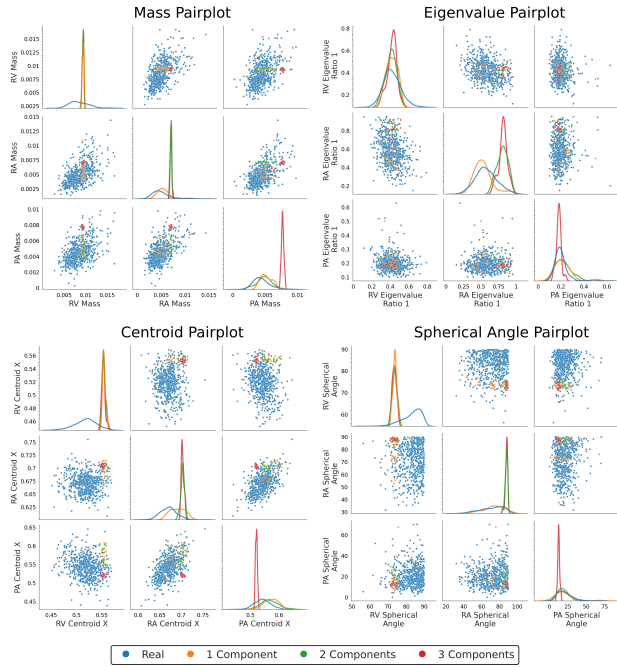


Figure 10: **Our guidance framework enables multi-part compositional generation.** Pair plot shows kernel density estimate plots (diagonals) and pairwise scatterplots (off-diagonals) for various morphological metrics. Guidance is applied to control the geometry of a varying number of labels, where a controlled metric induces a tall, peaked kernel density plot.

and left heart labels (6 components). For geometric guidance, we use our unconditional model and select the appropriate components Ω during guidance. For our baseline, we retrained the best conditional diffusion model (implicit) with 6 components using component-wise dropout. During baseline sampling we dropout all components that are unconstrained for various compo-

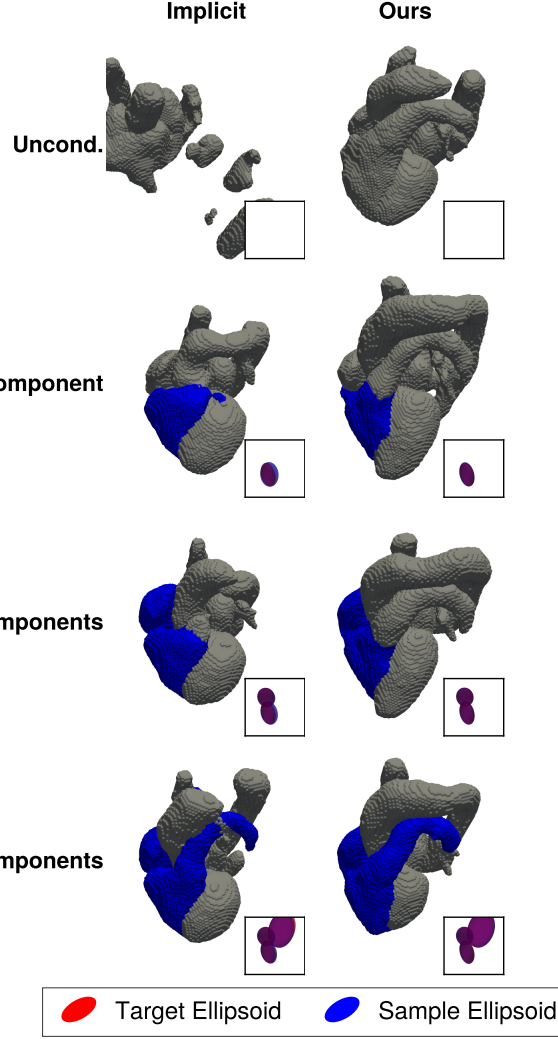


Figure 11: **Geometric guidance exhibits enhanced multi-part compositional generation when compared to a conditional drop-out baseline.** Columns show an implicit conditioning baseline against our method. Rows represent generating synthetic label maps based on constraining a varying number of voxel labels ■. The implicit baseline was trained using 6 components with dropout. To sample N components from the implicit model, we drop out $(6 - N)$ components during sampling.

ment counts (further details can be found in Section 8.6). Quantitative results can be seen in Table 2, which shows that with small number of constraining components, implicit conditioning with dropout fails to generate high-quality anatomy as measured by morphological and pointcloud metrics. Implicit models must therefore be retrained to constrain generation with a varying number of components. Conversely, when constrained

Table 2: Comparative analysis of various approaches for multi-component compositional generation. The number of components indicates the number of labels being actively constrained during sampling. MMD values are multiplied by 10^3 for ease of visualization.

No.	Cond.	Morph. Metrics			Pointcloud Metrics		
		Comp.	Method	FD (\downarrow)	Pr. (\uparrow)	Re. (\uparrow)	MMD (\downarrow)
0	Implicit	1622	0.00	0.99	55.7	0.288	0.915
	Ours	34.6	0.70	0.87	9.40	0.53	0.55
1	Implicit	227	0.00	0.87	17.1	0.40	0.79
	Ours	38.5	0.60	0.83	9.39	0.52	0.57
2	Implicit	57.6	0.54	0.84	10.6	0.50	0.65
	Ours	41.9	0.56	0.96	8.86	0.59	0.52
3	Implicit	29.8	0.80	0.81	9.21	0.48	0.58
	Ours	32.7	0.78	0.94	8.60	0.58	0.52
6	Implicit	31.1	0.82	0.95	8.11	0.56	0.50
	Ours	35.5	0.80	0.94	8.50	0.58	0.50

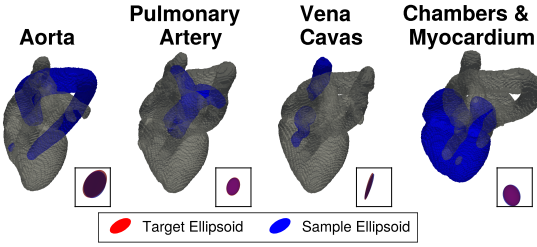


Figure 12: **Geometric guidance is compatible with structurally complex constraints.** We present qualitative results showing geometric control of labels that exhibit non-convex or branched structures.

with a higher number of components, the performance of implicit conditioning is similar to that of geometric guidance. This trend is observed qualitatively in Figure 11, where both methods show similar anatomical quality at high number of component constraints, but at a low number of components, only geometric guidance can generate realistic anatomy. We further show in Figure 10 how controlling multiple components within the right heart through geometric guidance can effectively sample from lower-dimensional slices of the original morphological distribution. Finally, we show in Figure 12 that our guidance framework can constrain the geometric attributes of structurally complex labels such as curved aortas, branching pulmonary arteries, as well as the boolean union of multiple labels such as both vena cavae or all four cardiac chambers.

5.8 Geometric Inpainting and Biophysical Simulations

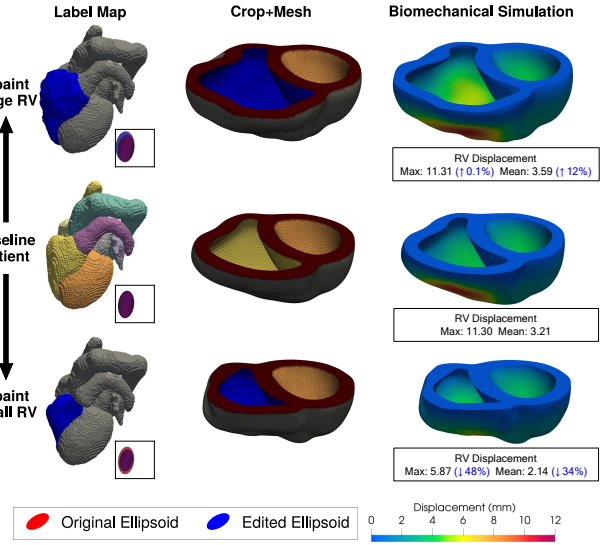


Figure 13: **Geometric guidance can controllably inpaint anatomical features for counterfactual biomechanical simulations.** Left column: a baseline patient being edited to have larger and smaller right ventricles where the gray voxels are unchanged during inpainting. Middle column: cropped biventricular mesh extracted from each scenario. Right column: editing the right ventricle size while retaining the left ventricle can modulate biomechanical outcomes.

We aim to demonstrate the capability of our geomet-

ric guidance framework to controllably and precisely inpaint patient-specific anatomies for simulation experiments. We set up a toy example involving biventricular pressurization, where we specifically aim to edit a patient-specific label map to enlarge or shrink the RV. This is demonstrated in Figure 13, where we extracted the RV moments and obtain the large RV targets by doubling the mass, and the small RV targets by halving the mass (left column insets). We then apply mask-based inpainting [15] to edit the RV with geometric guidance (left column) and crop out biventricular segmentations that are discretized with tetrahedral elements (middle column). We then simulate biventricular pressurization for the baseline patient case and digital siblings, showing that RV volume plays a significant role in determining wall displacement (right column). Further details on the cropping, meshing, and physical simulation steps can be found in Section 8.7.

6 Limitations

Our method has several limitations, for example, the relative weights of the geometric moments should be obtained through experimental tuning, similar to all guidance frameworks. Furthermore, in the case of empty segmentations, the position and shape losses can produce unstable gradients due to the mass being used in the denominator. In practise, this scenario can be easily detected mitigated through adaptive loss weightings. Lastly, anatomical diffusion models can generate topologically incorrect structures-such as disconnected aortas or several left atria, making the resulting simulation physics inaccurate. This can be addressed by filtering out topologically incorrect anatomies, at the cost of additional computational time. Future work should investigate topological regularization either during training or inference.

7 Conclusions

We present a flexible method to impose geometric constraints on diffusion models of 3D multi-component anatomical label maps. By measuring geometric moments relating to size, shape, and position during diffusion model sampling, we enable loss-based guidance without conditional training. We demonstrate that our framework can independently control geometric features such as size or shape, and constrain multiple anatomical components in a compositional manner. Our framework enables custom-tailoring realistic anatomy for computational simulation experiments, elucidating the causal relationships between form and simulated function.

References

- [1] Ali Sarrami-Foroushani, Toni Lassila, Michael MacRaild, Joshua Asquith, Kit CB Roes, James V Byrne, and Alejandro F Frangi. In-silico trial of intracranial flow diverters replicates and expands insights from conventional clinical trials. *Nature communications*, 12(1):3861, 2021.
- [2] Marco Viceconti, Luca Emili, Payman Afshari, Eulalie Courcelles, Cristina Curreli, Nele Famaey, Liesbet Geris, Marc Horner, Maria Cristina Jori, Alexander Kulesza, et al. Possible contexts of use for in silico trials methodologies: a consensus-based review. *IEEE Journal of Biomedical and Health Informatics*, 25(10):3977–3982, 2021.
- [3] Ehsan Abadi, William P Segars, Benjamin MW Tsui, Paul E Kinahan, Nick Bottenuis, Alejandro F Frangi, Andrew Maidment, Joseph Lo, and Ehsan Samei. Virtual clinical trials in medical imaging: a review. *Journal of Medical Imaging*, 7(4):042805–042805, 2020.
- [4] SA Niederer, Yasser Aboelkassem, Chris D Cantwell, Cesare Corrado, Sam Coveney, Elizabeth M Cherry, Tammo Delhaas, Flavio H Fenton, AV Panfilov, P Pathmanathan, et al. Creation and application of virtual patient cohorts of heart models. *Philosophical Transactions of the Royal Society A*, 378(2173):20190558, 2020.
- [5] Ross Straughan, Karim Kadry, Sahil A Parikh, Elazer R Edelman, and Farhad R Nezami. Fully automated construction of three-dimensional finite element simulations from optical coherence tomography. *Computers in Biology and Medicine*, 165:107341, 2023.
- [6] Caroline H Roney, Marianne L Beach, Arihant M Mehta, Iain Sim, Cesare Corrado, Rokas Bendikas, Jose A Solis-Lemus, Orod Razeghi, John Whitaker, Louisa O’Neill, et al. In silico comparison of left atrial ablation techniques that target the anatomical, structural, and electrical substrates of atrial fibrillation. *Frontiers in physiology*, 11:1145, 2020.
- [7] Qinxi Yu, Masoud Moghani, Karthik Dharmarajan, Vincent Schorp, William Chung-Ho Panitch, Jingzhou Liu, Kush Hari, Huang Huang, Mayank Mittal, Ken Goldberg, et al. Orbit-surgical: An open-simulation framework for learning surgical augmented dexterity. *arXiv preprint arXiv:2404.16027*, 2024.
- [8] Vivek Gopalakrishnan, Neel Dey, and Polina Golland. Intraoperative 2d/3d image registration via differentiable x-ray rendering. In *Proceedings of the IEEE/CVF Conference on Computer Vision and Pattern Recognition*, pages 11662–11672, 2024.
- [9] Vivek Gopalakrishnan and Polina Golland. Fast auto-differentiable digitally reconstructed radiographs for solving inverse problems in intraoperative imaging. In

- Workshop on Clinical Image-Based Procedures, pages 1–11. Springer, 2022.
- [10] Neel Dey, Benjamin Billot, Hallee E. Wong, Clinton Wang, Mengwei Ren, Ellen Grant, Adrian V Dalca, and Polina Golland. Learning general-purpose biomedical volume representations using randomized synthesis. In *The Thirteenth International Conference on Learning Representations*, 2025. URL <https://openreview.net/forum?id=x0mC5LiVuN>.
- [11] Benjamin Billot, Douglas N Greve, Oula Puonti, Axel Thielscher, Koen Van Leemput, Bruce Fischl, Adrian V Dalca, Juan Eugenio Iglesias, et al. Synthseg: Segmentation of brain mri scans of any contrast and resolution without retraining. *Medical image analysis*, 86:102789, 2023.
- [12] Virginia Fernandez, Walter Hugo Lopez Pinaya, Pedro Borges, Petru-Daniel Tudosiu, Mark S Graham, Tom Vercauteren, and M Jorge Cardoso. Can segmentation models be trained with fully synthetically generated data? In *Simulation and Synthesis in Medical Imaging: 7th International Workshop, SASHIMI 2022, Held in Conjunction with MICCAI 2022, Singapore, September 18, 2022, Proceedings*, pages 79–90. Springer, 2022.
- [13] Virginia Fernandez, Walter Hugo Lopez Pinaya, Pedro Borges, Mark S Graham, Petru-Daniel Tudosiu, Tom Vercauteren, and M Jorge Cardoso. Generating multi-pathological and multi-modal images and labels for brain mri. *Medical Image Analysis*, 97:103278, 2024.
- [14] Fanwei Kong, Sascha Stocker, Perry S Choi, Michael Ma, Daniel B Ennis, and Alison L Marsden. Sdf4chd: Generative modeling of cardiac anatomies with congenital heart defects. *Medical Image Analysis*, 97:103293, 2024.
- [15] Karim Kadry, Shreya Gupta, Farhad R Nezami, and Elazer R Edelman. Probing the limits and capabilities of diffusion models for the anatomic editing of digital twins. *npj Digital Medicine*, 7(1):1–12, 2024.
- [16] Karim Kadry, Shreya Gupta, Jonas Sogbadji, Michiel Schaap, Kersten Petersen, Takuya Mizukami, Carlos Collet, Farhad R Nezami, and Elazer R Edelman. A diffusion model for simulation ready coronary anatomy with morpho-skeletal control. In *European Conference on Computer Vision*, pages 396–412. Springer, 2025.
- [17] Enrico Fabris, Balasz Berta, Tomasz Roleder, Renicus S Hermanides, Alexander JJ IJsselmuiden, Floris Kauer, Fernando Alfonso, Clemens Von Birgelen, Javier Escaned, Cyril Camaro, et al. Thin-cap fibroatheroma rather than any lipid plaques increases the risk of cardiovascular events in diabetic patients: Insights from the combine oct–ffr trial. *Circulation: Cardiovascular Interventions*, 15(5):e011728, 2022.
- [18] Federica Sacco, Bruno Paun, Oriol Lehmkuhl, Tinen L Iles, Paul A Iaizzo, Guillaume Houzeaux, Mariano Vázquez, Constantine Butakoff, and Jazmin Aguado-Sierra. Left ventricular trabeculations decrease the wall shear stress and increase the intra-ventricular pressure drop in cfd simulations. *Frontiers in Physiology*, 9:458, 2018.
- [19] Brandon L Moore and Lakshmi Prasad Dasi. Coronary flow impacts aortic leaflet mechanics and aortic sinus hemodynamics. *Annals of biomedical engineering*, 43: 2231–2241, 2015.
- [20] Karim Kadry, Max L Olander, David Marlevi, Elazer R Edelman, and Farhad R Nezami. A platform for high-fidelity patient-specific structural modelling of atherosclerotic arteries: from intravascular imaging to three-dimensional stress distributions. *Journal of the Royal Society Interface*, 18(182):20210436, 2021.
- [21] Riddhish Bhalodia, Shireen Y Elhabian, Ladislav Kavan, and Ross T Whitaker. Deepssm: a deep learning framework for statistical shape modeling from raw images. In *Shape in Medical Imaging: International Workshop, ShapeMI 2018, Held in Conjunction with MICCAI 2018, Granada, Spain, September 20, 2018, Proceedings*, pages 244–257. Springer, 2018.
- [22] Fanwei Kong, Sascha Stocker, Perry S Choi, Michael Ma, Daniel B Ennis, and Alison L Marsden. Sdf4chd: Generative modeling of cardiac anatomies with congenital heart defects. *Medical Image Analysis*, 97:103293, 2024.
- [23] Karim Kadry, Max L Olander, Andreas Schuh, Abhishek Karmakar, Kersten Petersen, Michiel Schaap, David Marlevi, Adam UpdePac, Takuya Mizukami, Charles Taylor, et al. Morphology-based non-rigid registration of coronary computed tomography and intravascular images through virtual catheter path optimization. *IEEE Transactions on Medical Imaging*, 2024.
- [24] Mohamed Abdelkhalek, MohammadAli Daeian, and Zahra Keshavarz-Motamed. Regional assessment of aortic valve calcification using topographic maps in contrast-enhanced ct: In-vivo sex and severity-based differences in calcific presentation. *Quantitative Imaging in Medicine and Surgery*, 14(1):1, 2023.
- [25] Lisa R Pankewitz, Kristian G Hustad, Sachin Govil, James C Perry, Sanjeet Hegde, Renxiang Tang, Jeffrey H Omens, Alistair A Young, Andrew D McCulloch, and Hermenegild J Arevalo. A universal biventricular coordinate system incorporating valve annuli: Validation in congenital heart disease. *Medical Image Analysis*, 93:103091, 2024.
- [26] Mohammad Mostafa Asheghan, Hoda Javadikasgari, Taraneh Attary, Amir Rouhollahi, Ross Straughan,

- James Noel Willi, Rabina Awal, Ashraf Sabe, Kim I de la Cruz, and Farhad R Nezami. Predicting one-year left ventricular mass index regression following transcatheter aortic valve replacement in patients with severe aortic stenosis: A new era is coming. *Frontiers in Cardiovascular Medicine*, 10:1130152, 2023.
- [27] Masliza Mahmud, Kenneth Chan, Joao F Fernandes, Rina Ariga, Betty Raman, Ernesto Zacur, Ho-fon Royce Law, Marzia Rigolli, Jane M Francis, Sairia Dass, et al. Differentiating left ventricular remodeling in aortic stenosis from systemic hypertension. *Circulation: Cardiovascular Imaging*, 17(8):e016489, 2024.
- [28] Anthony A Gatti, Louis Blankemeier, Dave Van Veen, Brian Hargreaves, Scott L Delp, Garry E Gold, Feliks Kogan, and Akshay S Chaudhari. Shapemed-knee: A dataset and neural shape model benchmark for modeling 3d femurs. *medRxiv*, 2024.
- [29] Anna Corti, Marco Stefanati, Matteo Leccardi, Ovidio De Filippo, Alessandro Depaoli, Pietro Cerveri, Francesco Migliavacca, Valentina DA Corino, José F Rodriguez Matas, Luca Mainardi, et al. Predicting vulnerable coronary arteries: A combined radiomics-biomechanics approach. *Computer Methods and Programs in Biomedicine*, 260:108552, 2025.
- [30] Claire Conway, Farhad R Nezami, Campbell Rogers, Adam Groothuis, James C Squire, and Elazer R Edelman. Acute stent-induced endothelial denudation: biomechanical predictors of vascular injury. *Frontiers in Cardiovascular Medicine*, 8:733605, 2021.
- [31] Pengfei Dong, Hiram G Bezerra, David L Wilson, and Linxia Gu. Impact of calcium quantifications on stent expansions. *Journal of biomechanical engineering*, 141(2):021010, 2019.
- [32] Ali Madani, Ahmed Bakhaty, Jiwon Kim, Yara Mubarak, and Mohammad RK Mofrad. Bridging finite element and machine learning modeling: stress prediction of arterial walls in atherosclerosis. *Journal of biomechanical engineering*, 141(8):084502, 2019.
- [33] Reidmen Aróstica, David Nolte, Aaron Brown, Amadeus Gebauer, Elias Karabelas, Javiera Jilberto, Matteo Salvador, Michele Bucelli, Roberto Piersanti, Kasra Osouli, et al. A software benchmark for cardiac elastodynamics. *Computer Methods in Applied Mechanics and Engineering*, 435:117485, 2025.
- [34] Concetta Piazzese, M Chiara Carminati, Mauro Pepi, and Enrico G Caiani. Statistical shape models of the heart: applications to cardiac imaging. In *Statistical Shape and Deformation Analysis*, pages 445–480. Elsevier, 2017.
- [35] Marcel Beetz, Abhirup Banerjee, and Vicente Grau. Generating subpopulation-specific biventricular anatomy models using conditional point cloud variational autoencoders. In *International Workshop on Statistical Atlases and Computational Models of the Heart*, pages 75–83. Springer, 2021.
- [36] Haoran Dou, Seppo Virtanen, Nishant Ravikumar, and Alejandro F Frangi. A generative shape compositional framework: Towards representative populations of virtual heart chimaeras. *arXiv preprint arXiv:2210.01607*, 2022.
- [37] Jan Verhülsdonk, Thomas Grandits, Francisco Sahli Costabal, Rolf Krause, Angelo Auricchio, Gundolf Haase, Simone Pezzuto, and Alexander Effland. Shape of my heart: Cardiac models through learned signed distance functions. *arXiv preprint arXiv:2308.16568*, 2023.
- [38] Mengyun Qiao, Kathryn A McGurk, Shuo Wang, Paul M Matthews, Declan P O'Regan, and Wenjia Bai. A personalized time-resolved 3d mesh generative model for unveiling normal heart dynamics. *Nature Machine Intelligence*, pages 1–12, 2025.
- [39] Uxio Hermida, Milou PM van Poppel, Malak Sabry, Hamed Keramati, Johannes K Steinweg, John M Simpson, Trisha V Vigneswaran, Reza Razavi, Kuberan Pushparajah, David FA Lloyd, et al. The onset of coarctation of the aorta before birth: Mechanistic insights from fetal arch anatomy and haemodynamics. *Computers in Biology and Medicine*, 182:109077, 2024.
- [40] Jessica G Williams, David Marlevi, Jan L Bruse, Farhad R Nezami, Hamed Moradi, Ronald N Fortunato, Spandan Maiti, Marie Billaud, Elazer R Edelman, and Thomas G Gleason. Aortic dissection is determined by specific shape and hemodynamic interactions. *Annals of Biomedical Engineering*, 50(12):1771–1786, 2022.
- [41] Kenneth I Aycock, Tom Battisti, Ashley Peterson, Jiang Yao, Steven Kreuzer, Claudio Capelli, Sanjay Pant, Pras Pathmanathan, David M Hoganson, Steve M Levine, et al. Toward trustworthy medical device in silico clinical trials: a hierarchical framework for establishing credibility and strategies for overcoming key challenges. *Frontiers in Medicine*, 11:143372, 2024.
- [42] Jonathan Pham, Sofia Wyetzner, Martin R Pfaller, David W Parker, Doug L James, and Alison L Marsden. symorph: Interactive geometry-editing tools for virtual patient-specific vascular anatomies. *Journal of Biomechanical Engineering*, 145(3):031001, 2023.
- [43] Jonathan Pham, Fanwei Kong, Doug L James, and Alison L Marsden. Virtual shape-editing of patient-specific vascular models using regularized kelvinlets. *IEEE Transactions on Biomedical Engineering*, 2024.
- [44] Bram de Wilde, Max T Rietberg, Guillaume Lajoinie, and Jelmer M Wolterink. Steerable anatomical shape synthesis with implicit neural representations. *arXiv preprint arXiv:2504.03313*, 2025.

- [45] Weili Nie, Sifei Liu, Morteza Mardani, Chao Liu, Benjamin Eckart, and Arash Vahdat. Compositional text-to-image generation with dense blob representations. *arXiv preprint arXiv:2405.08246*, 2024.
- [46] Weixi Feng, Chao Liu, Sifei Liu, William Yang Wang, Arash Vahdat, and Weili Nie. Blobgen-vid: Compositional text-to-video generation with blob video representations. *arXiv preprint arXiv:2501.07647*, 2025.
- [47] Amir Hertz, Or Perel, Raja Giryes, Olga Sorkine-Hornung, and Daniel Cohen-Or. Spaghetti: Editing implicit shapes through part aware generation. *ACM Transactions on Graphics (TOG)*, 41(4):1–20, 2022.
- [48] Juil Koo, Seungwoo Yoo, Minh Hieu Nguyen, and Minhyuk Sung. Salad: Part-level latent diffusion for 3d shape generation and manipulation. In *Proceedings of the IEEE/CVF International Conference on Computer Vision*, pages 14441–14451, 2023.
- [49] Anonymous. Protcomposer: Compositional protein structure generation with 3d ellipsoids. In *Submitted to The Thirteenth International Conference on Learning Representations*, 2024. URL <https://openreview.net/forum?id=OctvBgKFgc>. under review.
- [50] Arpit Bansal, Hong-Min Chu, Avi Schwarzschild, Soumyadip Sengupta, Micah Goldblum, Jonas Geiping, and Tom Goldstein. Universal guidance for diffusion models. In *Proceedings of the IEEE/CVF Conference on Computer Vision and Pattern Recognition*, pages 843–852, 2023.
- [51] Yilun Du, Conor Durkan, Robin Strudel, Joshua B Tenenbaum, Sander Dieleman, Rob Fergus, Jascha Sohl-Dickstein, Arnaud Doucet, and Will Sussman Grathwohl. Reduce, reuse, recycle: Compositional generation with energy-based diffusion models and mcmc. In *International conference on machine learning*, pages 8489–8510. PMLR, 2023.
- [52] Dave Epstein, Allan Jabri, Ben Poole, Alexei Efros, and Aleksander Holynski. Diffusion self-guidance for controllable image generation. *Advances in Neural Information Processing Systems*, 36:16222–16239, 2023.
- [53] Hyungjin Chung, Jeongsol Kim, Michael Thompson Mccann, Marc Louis Klasky, and Jong Chul Ye. Diffusion posterior sampling for general noisy inverse problems. In *The Eleventh International Conference on Learning Representations*, 2023. URL <https://openreview.net/forum?id=OnD9zGAGT0k>.
- [54] Jakob Wasserthal, Hanns-Christian Breit, Manfred T Meyer, Maurice Pradella, Daniel Hinck, Alexander W Sauter, Tobias Heye, Daniel T Boll, Joshy Cyriac, Shan Yang, et al. Totalsegmentator: robust segmentation of 104 anatomic structures in ct images. *Radiology: Artificial Intelligence*, 5(5):e230024, 2023.
- [55] Robin Rombach, Andreas Blattmann, Dominik Lorenz, Patrick Esser, and Björn Ommer. High-resolution image synthesis with latent diffusion models. In *Proceedings of the IEEE/CVF Conference on Computer Vision and Pattern Recognition*, pages 10684–10695, 2022.
- [56] Jonathan Ho and Tim Salimans. Classifier-free diffusion guidance. *arXiv preprint arXiv:2207.12598*, 2022.
- [57] Tuomas Kynkänniemi, Tero Karras, Samuli Laine, Jaakko Lehtinen, and Timo Aila. Improved precision and recall metric for assessing generative models. *Advances in Neural Information Processing Systems*, 32, 2019.
- [58] Guandao Yang, Xun Huang, Zekun Hao, Ming-Yu Liu, Serge Belongie, and Bharath Hariharan. Pointflow: 3d point cloud generation with continuous normalizing flows. In *Proceedings of the IEEE/CVF international conference on computer vision*, pages 4541–4550, 2019.
- [59] Roy De Maesschalck, Delphine Jouan-Rimbaud, and Désiré L Massart. The mahalanobis distance. *Chemometrics and intelligent laboratory systems*, 50(1):1–18, 2000.
- [60] Jean Feydy, Thibault Séjourné, François-Xavier Vialard, Shun-ichi Amari, Alain Trouve, and Gabriel Peyré. Interpolating between optimal transport and mmd using sinkhorn divergences. In *The 22nd International Conference on Artificial Intelligence and Statistics*, pages 2681–2690, 2019.
- [61] SY Ho and P Nihoyannopoulos. Anatomy, echocardiography, and normal right ventricular dimensions. *Heart*, 92(suppl 1):i2–i13, 2006.
- [62] Shoaib A. Goraya, Shengzhe Ding, Mariam K. Arif, Hyunjoon Kong, and Arif Masud. Effect of circadian rhythm modulated blood flow on nanoparticle based targeted drug delivery in virtual in vivo arterial geometries. *Brain Multiphysics*, 7:100105, 2024. ISSN 2666-5220. doi: <https://doi.org/10.1016/j.brain.2024.100105>. URL <https://www.sciencedirect.com/science/article/pii/S2666522024000169>.
- [63] Soonpil Kang, JaeHyuk Kwack, and Arif Masud. Variational coupling of non-matching discretizations across finitely deforming fluid–structure interfaces. *International journal for numerical methods in fluids*, 94(6):678–718, 2022.

8 Appendix

8.1 Overview

- In Section 8.2 we provide details on dataset curation and processing.
- In Section 8.3 we provide implementation details for our autoencoder and diffusion model.
- In Section 8.4 we provide implementation details for our guidance algorithm.
- In Section 8.5 we provide implementation details for our conditional generation baselines.
- In Section 8.6 we provide further experimental details for both evaluation and inference.
- In Section 8.7 we provide implementation details for our biomechanical simulations.
- In Section 8.8 we provide additional details on the morphological plots for each experiment.

8.2 Dataset

For our study, we utilize TotalSegmentator v2 [54] to generate anatomical segmentations, with 596 cases manually selected based on segmentation quality assessment. Cardiac structures including the myocardium (Myo), left and right atria (LA & RA), left and right ventricles (LV & RV), aorta (Ao), and pulmonary artery (PA) were segmented using a specialized TotalSegmentator model trained on sub-millimeter resolution data. For the inferior vena cava (IVC), superior vena cava (SVC), and pulmonary veins (PV), we incorporate the labels from the original label map dataset. To ensure anatomical validity, we perform topological filtration on all structures except the pulmonary veins, where we extract only the largest connected component. The resulting segmentations are standardized by resampling to a uniform voxel resolution of 2mm and subsequently cropped. The crop center is determined from the union of all four chamber segmentations, and the crop length is set to 128 voxels for each side.

8.3 Latent Diffusion Model Implementation

For this study, we adapt the VAE and LDM architectures specified by Kadry et al. [15]. The number of input and output channels of the Variational Autoencoder (VAE) is set to 11, corresponding to 10 distinct cardiac labels along with an additional channel for the background. The number of input channels for the

LDM is set to 3 for unconditional sampling. The hyperparameters and training configuration for the VAE and LDM are contained in Table 3 and Table 4 respectively.

Table 3: Autoencoder hyperparameters

Hyperparameter	Value
lr	1×10^{-5}
Epochs	40
Batch Size	1
Num. Channels	[16,32,64]
Num. Res. Blocks	2
Downscaling Factor	4
Recon. Loss Weight	1
KL Weight	1×10^{-6}

Table 4: Diffusion model hyperparameters

Hyperparameter	Value
Training	
lr	2.5×10^{-5}
Epochs	50
Batch Size	1
Num. Channels	[64, 128, 196]
Num. Res. Blocks	2
Num. Attn. Heads	1
Attn. Res.	8, 4, 2
σ_{data}	1
$p(\sigma)$ mean	1
$p(\sigma)$ std	1.2
Sampling	
σ_{\min}	1×10^{-2}
σ_{\max}	80
ρ	3

8.4 Geometric Guidance Implementation

8.4.1 Guidance Weight Tuning

We determine the optimum weight factors $\lambda = [\lambda_0, \lambda_1, \lambda_2]$ for our geometric loss through tuning each loss in isolation. We specifically optimize conditional fidelity while retaining generation quality metrics. The final weight values can be seen in Table 5.

8.4.2 Guidance Implementation

To ensure that the extracted components yield interpretable moments, we require the voxel grid values to be softly binarized, with one tissue channel approaching 1 while the others are close to 0. To achieve this, we apply a softmax function with a temperature of 10^{-2} . During

the computation of geometric moments, we observed that segmentations that are empty or nearly empty, particularly those with small components, lead to unstable gradients that significantly degrade the quality of generation. This instability arises because the centroid and covariance loss calculations utilize mass in the denominator. To mitigate this issue, we introduce a small amount of noise to the mass term whenever it appears in the denominator, thereby stabilizing the overall process. After computing all moments, we normalize the mass term by the total number of voxels such that the term represents volume fraction. Unless stated otherwise, we use 50 denoising steps for all generated samples.

Table 5: Geometric moment losses and their corresponding weight factors.

Guidance Loss	Weight Factor λ
$\mathcal{L}_{\text{size}}$	10^7
\mathcal{L}_{pos}	10^5
$\mathcal{L}_{\text{shape}}$	10^4

8.5 Baseline Methods Implementation

- **Explicit Conditioning:** To ensure that the elements of \mathcal{G}_{exp} are roughly between 0 and 1, we min-max normalize the masses \mathcal{M} , centroids \mathcal{C} , and normalized covariances \mathcal{S}_n with values calculated from the real dataset (Table 6). The input channels for the latent diffusion model are increased to handle the concatenated input. does not readily permit the use of dropout to train a diffusion model in an unconditional manner because the null condition is defined as zero—equivalent to the minimum moment values. We include explicit conditioning results for guidance weights smaller than 0 in Figure 4 for completeness.
- **Cross-Attention Conditioning:** Our initial tokens consist of 13-dimensional vectors representing the concatenation of mass \mathcal{M} , centroids \mathcal{C} , and normalized covariances \mathcal{S}_n . The tokens are then min-max normalized similar to explicit conditioning and embedded into a 256 dimensional vector for cross-attention. To embed the component index, we use a linear embedding layer. To embed the geometric moments, we use an MLP with three linear layers and 2 ReLU layers bewteen layers 1 and 2. Both embeddings are added together and used to condition the U-Net with cross-attention, where we use 8 attention heads. To enable unconditional

generation, we randomly dropout each channel of $\mathcal{G}_{\text{cross}}$ with a probability of 0.1.

- **Implicit Conditioning:** To compute the ellipsoidal distance map, we use the centroids \mathcal{C} and non-normalized covariances \mathcal{S} for each component to compute the Mahalanobis distance [59] for each voxel position. We then apply a shifted sigmoid transform—with a slope of -0.5 and a bias of 1—to constrain the outputs between 0 and 1, and subsequently concatenate the resulting grid to the latents. To enable unconditional generation, we randomly dropout each channel of \mathcal{G}_{imp} with a probability of 0.1. One limitation of this approach is that the target mass can only be targeted indirectly through the non-normalized covariance term, which can be seen in the conditional fidelity plot for size in Figure 4.

Table 6: Normalizing constants for geometric moments during explicit and cross-attention based conditioning.

Geometric Moment	Normalizing Minimum	Normalizing Maximum
\mathcal{M}	3.19×10^{-3}	1.3×10^{-2}
\mathcal{C}	0	1
\mathcal{S}	-1×10^{-4}	1×10^{-2}

8.6 Additional Experimental Details

- **Morphological evaluation metrics:** To compute the morphological metrics, the features are normalized by the mean and standard deviation of the real data. To calculate precision and recall, we use a nearest neighbors value of 5.
- **Pointcloud evaluation metrics** To compute the point cloud metrics for each segmentation, we calculate MMD, COV, and NNA for every tissue label using 256 points sampled using farthest point sampling. The values are then averaged over the number of components. To compute the pointcloud distances, we use the Earth Mover’s Distance (EMD) as computed through the Sinkhorn divergence [60].
- **Disentangled Generation:** Disentangled generation is done by zeroing out all but one of the geometric moment losses. Exact configuration details are shown in Table 7. We use 50 denoising steps for all generated samples.
- **Compositional Generation:** Our compositional generation experiments vary the number of components that constrain the generation process. The

exact labels used for each experiment are detailed in Table 8. We use 100 denoising steps for all generated samples.

Table 7: Configuration details for the disentangled generation ablation study. Checkmarks \checkmark indicate the associated weight factor λ_i is active while \times indicates the weighting factor is zeroed out.

Guidance Loss	λ_0	λ_1	λ_2
Uncond.	\times	\times	\times
$\mathcal{L}_{\text{size}}$	\checkmark	\times	\times
\mathcal{L}_{pos}	\times	\checkmark	\times
$\mathcal{L}_{\text{shape}}$	\times	\times	\checkmark
$\mathcal{L}_{\text{geom}}$	\checkmark	\checkmark	\checkmark

Table 8: Configuration details for the compositional generation study. Each component number corresponds to a set of labels that were constrained during generation

Components	Labels
0	None
1	RV
2	RV, RA
3	RV, RA, PA
6	RV, RA, PA, LV, LA, Ao

8.7 Biomechanical Simulation Details

- **Biventricular Cropping:** As only myocardial tissue is available for the left ventricle, we expand a myocardium mask around the right ventricle, assuming a constant thickness of 4 mm (2 voxels) corresponding to the clinical literature [61]. To crop the left and right ventricles at the base of the heart, we define a vector going from the LV centroid to the LA centroid, and crop the ventricles by adjusting the position threshold along the defined direction.
- **Tetrahedral Meshing and Processing:** The segmentation is then converted into a surface mesh using marching cubes, with a voxel-wise scale of 2 mm. Tetrahedral mesh generation is performed using the open-source software **GMSH** and **MeshLab**. The three anatomical models, large RV, baseline patient, and small RV (Fig. 13), are discretized into 39,780, 42,768, and 47,347 linear tetrahedral elements, respectively, with an average edge length of 2 mm.

- **Pressurization Simulation:** An in-house Finite element method (FEM) solver, implemented in **Fortran** with **MPI**, is used for the simulations. The solver is based on the variational multiscale method, providing stabilized FEM formulations [62, 63]. Simulation results are visualized using the open-source package **ParaView**.

The myocardium is modeled as a standard neo-Hookean material with a Young’s modulus of 25 kPa and a Poisson’s ratio of 0.4. Physiological pressure loads of 12 mmHg and 6 mmHg were applied to the LV and RV endocardium, respectively, corresponding to normal diastolic blood pressure. To constrain rigid body motion, zero-displacement Dirichlet boundary conditions are imposed at the base of the heart, while a stress-free Neumann boundary condition is enforced on the pericardium.

The nonlinear finite-deformation elasticity problem is then solved using the Newton–Raphson (NR) method. A direct solver (**MUMPS**) is employed to solve the discretized algebraic system at each NR iteration, with a convergence tolerance set to 10^{-20} for the initial residual. Simulations are carried out on a cluster using 128 parallel processors.

8.8 Morphological Analysis Details

We illustrate the effects of geometric guidance, disentangled generation, and compositional generation through morphological plots, where we plot each anatomical component in terms of representative quantities for size, shape, and position.

For size, we plot the mass of each component. Position is represented by the centroidal x-coordinate. To characterize shape, we extract the largest principal component and its associated eigenvector from the covariance matrix. We also plot the spherical angle (defined as the polar angle) to represent orientation, and the ratio between the largest eigenvalue and the second-largest eigenvalue to represent elongation.